ACS OMEGA

http://pubs.acs.org/journal/acsodf

Article

Quaternary Cu_2FeSnS_4/PVP/rGO Composite for Supercapacitor Applications

Melkiyur Isacfranklin, Rathinam Yuvakkumar,* Ganesan Ravi,* Balasubramaniam Saravanakumar, Mehboobali Pannipara, Abdullah G. Al-Sehemi, and Dhayalan Velauthapillai*

Cite This: *ACS Omega* 2021, 6, 9471−9481

Read Online

ACCESS | Metrics & More | Article Recommendations

ABSTRACT: Electrochemical energy storage is a current research area to address energy challenges of the modern world. The Cu_2FeSnS_4/PVP/rGO-decorated nanocomposite using PVP as the surface ligand was explored in a simple one-step solvothermal route, for studying their electrochemical behavior by designing asymmetric hybrid supercapacitor devices. The full cell three-electrode arrangements delivered 748 C/g (62.36 mA h/g) at 5 mV/s employing CV and 328 F/g (45.55 mA h/g) at 0.5 A/g employing GCD for the Cu_2FeSnS_4/PVP/rGO electrode. The half-cell two-electrode device can endow with 73 W h/kg and 749 W/kg at 1 A/g energy and power density. Furthermore, two Cu_2FeSnS_4/PVP/rGO//AC asymmetric devices connected in series for illuminating a commercial red LED more than 1 min were explored. This work focuses the potential use of transition-metal chalcogenide composite and introduces a new material for designing high-performance supercapacitor applications.

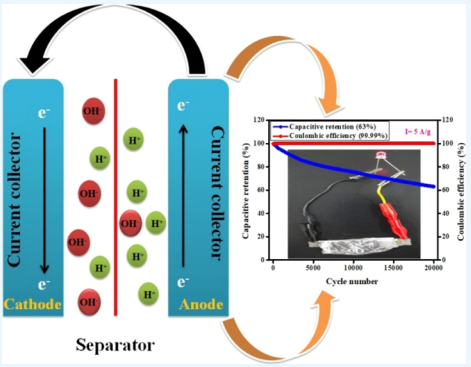

1. INTRODUCTION

In the developing modern era, the world is facing great hardships as fuel prices continue to rise, air pollution continues to rise, and fossil fuels become inadequate. In such a scenario, the so-called unconventional energies should be used to meet energy requirements.[1,2] The one of the drawback is that there is no sustainable storage source to store such energies. Supercapacitors and batteries are a potential source of energies for practical use, while principle energy sources can be exhausted.[3,4] Recently, supercapacitors have attracted a lot of interest due to their physicochemical characteristics because of double-layer capacitor (EDLC) or pseudocapacitor charge-storage mechanisms.[5,6] Pseudocapacitors are having high storage and on the other hand having low cyclic rate, whereas EDLC materials as carbon-based electrode materials exhibit excellent cyclability.[7−9] Nanomaterials are widely used to provide alternative energy sources to eco-friendly fossil fuels. For example, various alloys, metal nitrides, metal oxides, and sulfides have been used for supercapacitor use.[10,15] Generally, NiO, SnO, MnO_2, RuO_2, V_2O_5, and Co_3O_4 and their composites are used as electrode materials.[11,12] So far, RuO_2 has been reported as the best electrode material that can provide good performances due to its excellent theoretical specific capacity (1400−2000 F/g). Nevertheless, the high cost of production and the effects of agglomeration stand as high barriers for marketable use.[13] Nowadays, the binary, ternary, and quaternary transition-metal composites are extensively investigated to improve the specific capacity and the performance of the supercapacitor. In recent days, research studies have been carried out on quaternary chalcogenides for its excellent redox activity, pseudocapacitance, and effective layering ion diffusion.[14,15] It is a good idea to try and use the Cu_2FeSnS_4 material with the earth's numerous replacement for the supercapacitor application which are tetrahedral integrated systems, wherein every sulfur anion is bound with 4 cations and vice versa.[16] Numerous protocols are being accounted to synthesize Cu_2-II−IV−VI_4 group semiconductor materials in literature studies.[17] According to the literature review, no similar efforts have been carried out for using such a composition in supercapacitor applications.[18] Nanostructures greatly enhanced supercapacitor applications because of the suitable addition of carbon-based materials. Thus, improving ionic transport at the electrode/electrolyte interface accelerates redox reactions that occur in energy-harvesting devices. The earth-abundant quaternary chalcogenide materials are rarely reported in the supercapacitor applications. Furthermore, in stability point of view, the sulfide materials easily decayed in the aqueous electrolytes. Accordingly, retaining the stability is a curial factor in supercapacitor applications. The novel

Received: December 18, 2020
Accepted: March 5, 2021
Published: March 30, 2021

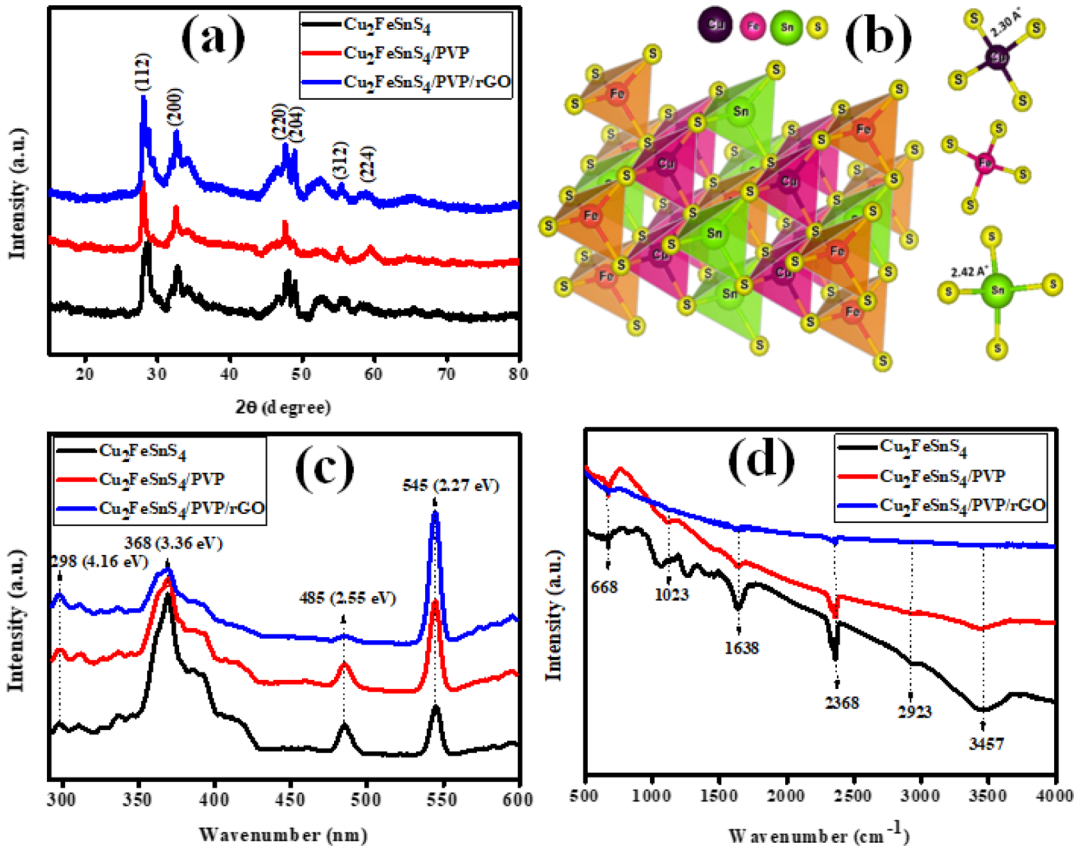

Figure 1. (a) XRD, (b) crystallographic, (c) PL, and (d) FTIR spectra of Cu_2FeSnS_4/PVP/rGO.

combination of Cu_2FeSnS_4/PVP/rGO focuses the long-term stability in the two-electrode system up to 2000 cycles. Also, this work highlighted an alternative electrode with a novel composite to enhance the electrochemical performances. This work definitely grasps the attention of the all researchers working in the areas of energy-related applications.

2. MATERIALS AND METHODS

Preparation of GO and rGO was followed by the modified Hummer's method. First, 0.6 g of graphite flakes was blended with 23 mL of H_2SO_4 and stirred well for an hour. Then, in an ice bath, the mixture was stirred for 30 min and 3 g of potassium permanganate was added. After that, 46 mL of double-distilled water was diluted with the resulting solution. Then, temperature was increased rapidly to 100 °C and the appearance of the color was changed to brown. Finally, the yellow color appeared after the addition of 10 mL of hydrogen peroxide (H_2O_2). The sediment was desiccated at 100 °C for 12 h to obtain the GO product, and then, 100 mg of GO was mixed with 100 mL of water. After that, 500 mg of $NaBH_4$ was appended and stirred at room temperature for 12 h. The reduced GO was gradually obtained.[19] In the synthesis process of Cu_2FeSnS_4, Cu_2FeSnS_4/PVP, and Cu_2FeSnS_4/PVP/rGO, initially, 0.1 M copper (II) chloride dehydrate, 0.05 M ferric chloride anhydrous, and 0.05 M tin (IV) chloride pentahydrate were suspended in 80 mL of water and stirred continuously for 30 min and found to be greenish brown. Then, a 0.4 M thiourea sulfide source was mixed in the abovementioned solution and stirred for another 1 h. The abovementioned mixture was then poured into a 100 mL autoclave at 160 °C for 12 h. Finally, the Cu_2FeSnS_4 product was obtained. Subsequently, a similar procedure was followed for the addition of polyvinyl pyrrolidone (PVP) as a structure-directing reagent in the chemical process to regulate crystal growth and nucleation, reducing surface tension and stabilizing metal nanoparticles. Third, the RGO was dispersed into the Cu_2FeSnS_4/PVP compound to form another compound called Cu_2FeSnS_4/PVP/rGO. Subsequently, the obtained Cu_2FeSnS_4, Cu_2FeSnS_4/PVP, and Cu_2FeSnS_4/PVP/rGO powders were given for characterization, and electrochemical performance was carried out for all samples.[20] The Cu_2FeSnS_4 compound was formed by dissolving water in metal chlorides and precursors of thiourea, and necessary chemical reactions during the synthesis of materials are described.[32,36]

$$CuCl_2 \rightarrow Cu^{2+} + 2Cl^-; \qquad FeCl_2 \rightarrow Fe^{2+} + 2Cl^-;$$
$$SnCl_4 \rightarrow Sn^{4+} + 4Cl^-$$

$$CS(NH_2)_2 \rightarrow S^{2-} + Ha + NH_2 - CaNH$$

$$CuCl_2 + FeCl_2 + CS(NH_2)_2 \rightarrow [CuFeSn(CS(NH_2)_n]^{m+}$$

The chemical composition of Cu/Fe/Sn/S is 2:1:1:4 M.

$$2Cu^{2+} + Sn^{2+} \rightarrow 2Cu^{+} + Sn^{4+}$$

$$Cu^{+} + en \rightarrow [Cu(en)]^{+};$$
$$Fe^{2+} + en \rightarrow [Fe(en)]^{2+};$$
$$Sn^{4+} + en \rightarrow [Sn(en)]^{4+}$$

$$(NH_2)_2CS + 2H_2O \rightarrow S^{2-} + 2NH^{4+} + CO_2\uparrow$$

https://doi.org/10.1021/acsomega.0c06167
ACS Omega 2021, 6, 9471−9481

$$2[Cu(en)]^{+} + [Fe(en)]^{2+} + [Sn(en)]^{4+} + 4S^{2-} \rightarrow Cu_2FeSnS_4$$

For electrochemical measurements and electrode preparations, Cu_2FeSnS_4 (80%) was mixed with activated charcoal (10%), acetylene black (5%), polyvinylidene fluoride (PVDF) (5%), and solution of binder in *N*-methyl-2-pyrrolidone (NMP) on nickel foam. Filter paper soaked in 2 M potassium hydroxide was used as a separator. An asymmetric cell was constructed with 2 M KOH with Cu_2FeSnS_4 and AC as positive and negative electrodes which were separated by KOH-soaked filter paper configuration to form a supercapacitor. The two-electrode cell system was configured as follows: Cu_2FeSnS_4/PVP/rGO||2 M KOH||AC using biological SP-150 instruments. The following mathematical relationship explored to calculate

$$\text{specific capacity from CV: } C_s = \int \frac{I \times dv}{2 \times s \times \Delta V \times m} \text{C/g} \quad (1)$$

$$\text{specific capacitance from GCD: } C_s = \frac{I \times \Delta t}{m \times \Delta v} \text{F/g} \quad (2)$$

It is necessary to specify capacitance in F/g to the specific capacity in C/g or mA h/g to show battery-like behavior.

$$\text{specific capacity from CV: } C = \frac{\int I \times dv}{2 \times 3.6 \times \Delta V \times m} (\text{mA h/g}) \quad (3)$$

$$\text{specific capacity from GCD: } C_s = \frac{I \times \Delta t}{3.6 \times m} (\text{mA h/g}) \quad (4)$$

To fabricate the hybrid ASC supercapacitor, Cu_2FeSnS_4/rGO as a cathode and AC as an anode were used to explore Cu_2FeSnS_4/rGO//AC. The cathode electrode was designed by blending 80:10:5:5 wt % of active material, activated carbon, acetylene black, and polyvinylidene fluoride (PVDF), respectively. The anode electrode was the combination of activated carbon (80 wt %), acetylene black (10 wt %), and polyvinylidene fluoride (PVDF) (10 wt %) using *N*-methyl pyrrolidone as a solvent. All the material mingled well to make slurry. Thereafter, the mixture was coated uniformly on Ni foam (1 × 1 cm^2) and vacuum air-dried at 80 °C. The charge balancing was optimized by proper mass proportion of the cathode and anode; $m_+/m_- = Q_-/Q_+ \times V_-/V_+$. To calculate the specific capacity, energy, and power density, one can employ the following formula.[21,22]

$$E = \frac{C \times \Delta V^2}{7.2} (\text{W h/g}) \quad (5)$$

$$P = \frac{3600 \times E}{\Delta t} (\text{W/kg}) \quad (6)$$

3. RESULTS AND DISCUSSION

The XRD diffraction pattern of the synthesized pure Cu_2FeSnS_4 and the addition of PVP and rGO are explored in Figure 1a (JCPDS 44-1476). The formation of (112), (200), (220), (204), (312), and (224) planes in the corresponding diffraction peaks in all the samples suggested the formation of the well-crystallized Cu_2FeSnS_4 orthogonal structure. No other secondary diffraction peaks were observed. The Scherrer formula $D = 0.89\ \lambda/\beta \cos\theta$ was used and the crystallite size of 27 nm was calculated for the high intensity diffraction pattern of the (112) plane. The dislocation density $\delta = 1.37 \times 10^{15}$ lines/meter^2 and microstrain $\varepsilon = 1.28 \times 10^{-3}$ were calculated for the high intensity $2\theta = 28.40°$ peak using the respective formulas $\delta = 1/D^2$ and $\varepsilon = \beta \cos\theta/4$.[23] Figure 1b reveals the crystallographic image of the Cu_2FeSnS_4 using the Vesta software.

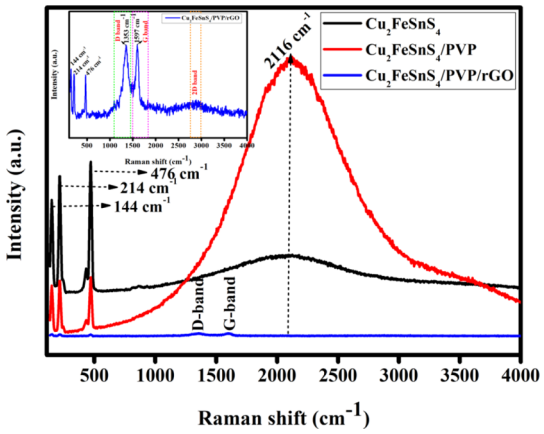

Figure 2. Raman spectra of Cu_2FeSnS_4/PVP/rGO.

Figure 1c reveals the photoluminescence spectra of pure Cu_2FeSnS_4 and the addition of PVP and rGO samples under an excitation wavelength of 270 nm. The PL spectra displayed strong peaks centered at 545 and 368 nm and the weak peaks centered around 485 and 298 nm; 368 nm may be because of band-to-band transition. The peak assigned to 545 nm in the visible region is the reason for the surface defects during the growth process. Also, the emission occurred in the visible region may be the cause of oxygen vacancies and the recombination of electron trapping in the crystal interstitials. The green emission at 485 nm is because of surface vacancies which may be because of electron transition. The absorption peak at 298 nm is attributed to the quantum effect related to the copper sulfide.[24,25] The infrared spectrum explored the ion state in a crystal due to crystal vibrations, as displayed in Figure 1d. Vibrations of the infrared absorption group in solids typically occur at 100−1000; 668 cm^{-1} indicates stretching vibration of the metal−thiourea complex-C−S of the synthesized product. The band located at 1020 cm^{-1} also denotes stretching vibration of the C−S band. The 1638 cm^{-1} band is responsible for the metal−thiourea complex-N−C−N stretching and NH_2 bending vibrational mode. The carbon-dioxide peak is revealed at 2368 cm^{-1}. The peak at 3467 cm^{-1} is attributed to O−H stretching vibration of H_2O.[26]

The identification of the various compositional phases of the synthesized material has been revealed through the Raman studies (Figure 2). The characteristic Raman vibrational modes are observed at 144, 214, 476, and 2116 cm^{-1}. In the Cu_2FeSnS_4/PVP/rGO product, the formation of the D and G band and 2D bands is located at 1353, 1597, and 2400−2500 cm^{-1}. The peak at 476 cm^{-1} revealed the sulphur S−S mode. The peak assigned to 214 cm^{-1} is corresponding to the pure sulfur anion in the region of the copper metal.[27] The disorder-induced D band and first-order graphite G band (I_D/I_G) ratio is used to measure disorder. Intensity is proportional to disorder. In our case, the $I_D/I_G = 0.99$ explored nanocrystalline graphitic nature. The peak at 1353 cm^{-1} attributed to the D

https://doi.org/10.1021/acsomega.0c06167
ACS Omega 2021, 6, 9471−9481

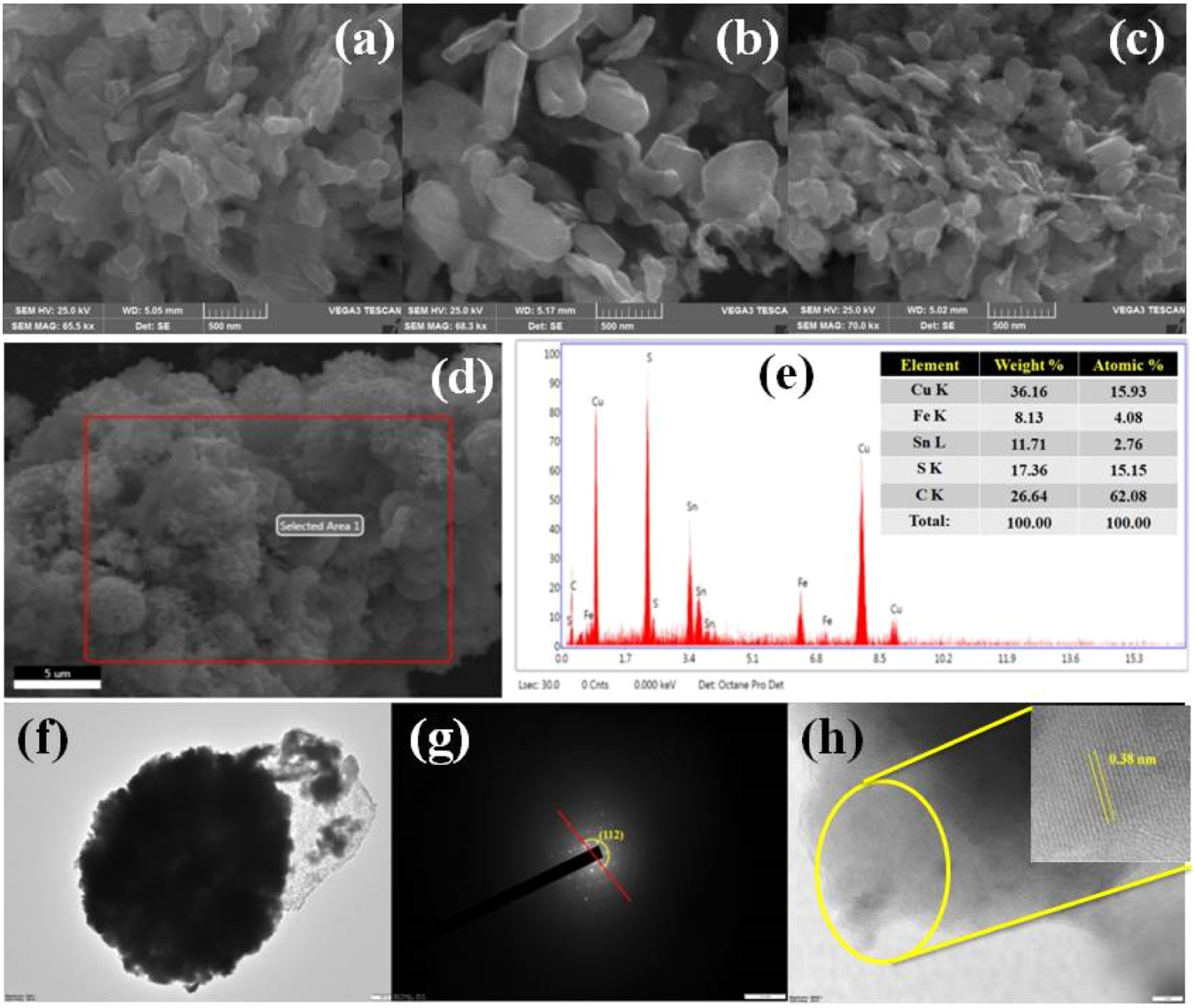

Figure 3. (a–c) SEM images, (d) EDS scanned area, (e) EDAX mapping, and (f–h) TEM images with the SAED pattern of Cu_2FeSnS_4/PVP/rGO.

band refer to defective sites with vacancies and grain boundaries and the G band at 1597 cm^{-1} responsible for o E_{2g} phonon first-order scattering of the sp^2 carbon–carbon bond.[28]

Figure 3a–c reveals SEM micrographs of synthesized Cu_2FeSnS_4 nanostructures among the addition of PVP and rGO. Almost all the morphological images exhibit agglomerated nanoparticles. It is clearly evidenced with the average 200 nm size. The surface ligand PVP had a major impact on the nucleation and growth.[29] Figure 3d shows the selected area of the EDS spectrum which clearly evidenced the formation of sphere-like morphological structures. The EDAX mapping with the atomic and weight percentages of Cu_2FeSnS_4/PVP/rGO is shown in Figure 3e. Figure 3f–h reveals TEM analysis of the Cu_2FeSnS_4/PVP/rGO sample. The clear-cut spherical ball-structured morphology along with the nanosheet is due to rGO content confirmed through the TEM analysis with the SAED pattern of a series of diffraction rings. The crystal plane of (112) was marked in the SAED pattern, and the gap between the fringes is around 0.38 nm.[30] The carbon-based rGO products were combined with these quarterly products formed between surface and graphene layers. rGO dispersed with Cu_2FeSnS_4/PVP facilitates electrolyte diffusion through their electrodes and reduces product internal resistance; as a result, the conductivity has been greatly improved.

The surface composition of synthesized Cu_2FeSnS_4/PVP/rGO nanostructures has been explored. Figure 4a reveals the survey spectrum of the prepared product. Peaks located at 931.30 and 951.16 eV are attributed to the $Cu2P_{3/2}$ and $Cu2P_{1/2}$ species. The peak splitting of 19.31 eV denotes the Cu(I) configuration (Figure 4b). The most popular peaks at 709.60 eV ($Fe2p_{3/2}$) and 724.42 eV ($Fe2p_{1/2}$) signify the Fe(II) configuration, and the peak centered at 715.60 is responsible for $Sn2p_{3/2}$ (Figure 4c). 485.60 and 494 eV correspond to $Sn3d_{5/2}$ and $Sn3d_{3/2}$, as displayed in Figure 4d, which specifies the Sn(IV) configuration. The peak expected at 160–164 eV is corresponding to the sulfide phases. The single peak in Figure 4e at 161.32 eV is the reason for the Sn(−II) oxidation state. Finally, the carbon peaks are positioned at 283.66 eV for C1s which could be the reason for the presence of rGO in the synthesized material, as displayed in Figure 4f.

https://doi.org/10.1021/acsomega.0c06167
ACS Omega 2021, 6, 9471–9481

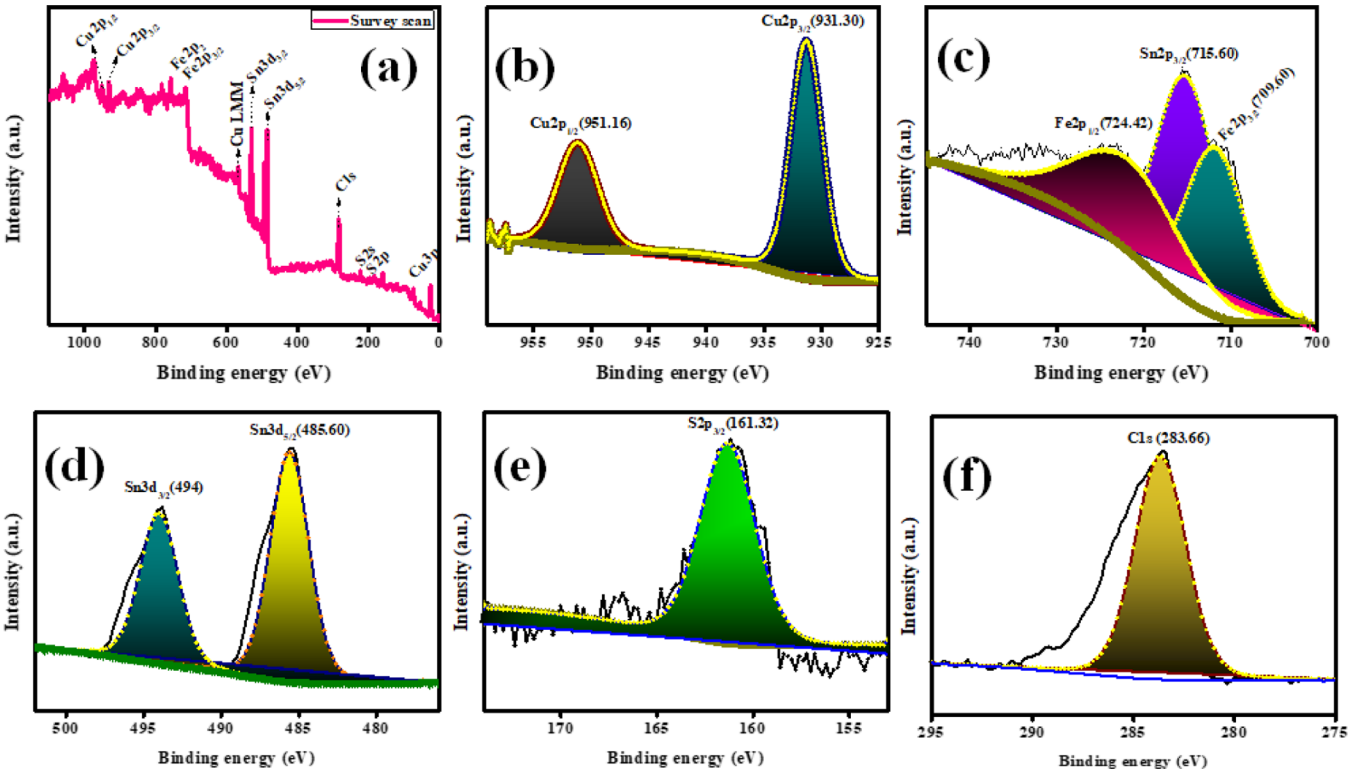

Figure 4. (a–f) XPS analysis of Cu_2FeSnS_4/PVP/rGO.

The major states of the Cu, Fe, Sn, and S elements are +1, +2, +4, and −2, for Cu_2FeSnS_4 chemical formula.[31]

Electrochemical processes were studied at 2 M KOH to test electrochemical behavior. Cyclic voltammetry (CV) is an electrochemical tool commonly used to reveal oxidation and reduction processes of molecular species, electrochemical reactions caused by the electron transfer process, and the performances of the supercapacitor. In the CV technique, current is recorded when the electric potential varies with the corresponding scan rates. Figure 5a–c reveals the CV graphs of the prepared Cu_2FeSnS_4 and its composite at different sweep currents (5–50 mV/s) in 0–0.6 V. Pseudocapacitors store charges by the active substance surface redox reaction and OH^- ions in the KOH solution. Charge is stored for the electric double layer at the electrode–electrolyte interface. As a result of the current responses, a pair of redox peaks clearly express battery-type properties, resulting in electrode materials showing reversible Faradaic reactions. Faradaic redox reactions of charge-storage mechanisms are as follows: $Cu_2FeSnS_4 + 9OH^- \rightarrow 2Cu(OH)_2 + M(SOH) + Sn(OH)_4 + 3S$, where M signifies Fe. The CV profiles of Cu_2FeSnS_4 explored the active redox pairs of Cu^+/Cu^{2+}, Fe^{2+}/Fe^{3+}, and Sn^{2+}/Sn^{4+} operating in a constant-potential window of OH anions in an alkaline electrolyte.[32] The electrochemical redox reaction occurs only when the electrons are transmitted from a Ni foam substrate that is oxidized to one that is being reduced. Almost all CV curves revealed similar patterns of current responses (redox peaks), while increasing the scan rate except for systematic anodic and cathodic shifts in the positive and negative directions, respectively, because of the fast Faradaic reaction. Electrolyte ion diffusion is indicated by opposition of peak shift at low potential. These CV results should be consistent with the electrochemical reactions at a high scan rate. The behavior of these redox reactions ensures that the appropriate chosen electrode can provide better reversibility.[33] Hence, it shows the battery-type behavior, and the specific capacity was calculated for the synthesized product using eq 1. The calculated specific capacity values are 398 C/g (33.19 mA h/g), 602 C/g (50.13 mA h/g), and 748 C/g (62.36 mA h/g) at a 5 mV/s scan rate for Cu_2FeSnS_4, Cu_2FeSnS_4/PVP, and Cu_2FeSnS_4/PVP/rGO, respectively, and the remaining specific capacity values of all other scan rates are pictorially illustrated (Figure 5g).

The electrode materials are also determined by charge–discharge capabilities by varying different current densities (Figure 4d–f). The calculated values are 139 F/g (19.30 mA h/g), 259 F/g (34.72 mA h/g), and 328 F/g (45.55 mA h/g) at 0.5 A/g for Cu_2FeSnS_4, Cu_2FeSnS_4/PVP, and Cu_2FeSnS_4/PVP/rGO, respectively, and all other specific capacitance values are illustrated (Figure 5h). The capacitance decrease is proportional to current density increase as a result of scan rate and redox reaction in the CV. At high current densities, only outer active electrode surface is used for redox reactions which may be due to time limitations. Nevertheless, low current density is used for the entire inner and outer electrode surface to promote efficient redox activity. Due to the lack of sufficient electrolyte ions in the higher current densities, it does not have sufficient reactive kinetics to migrate and diffuse the electrolyte ions to the electrodes. Further IR losses and concentration polarization may be in addition to the decrease in capacitance of the high current density. Galvanostatic charge–dischare (GCD) curves are similar to curves at EDLC electrodes, with a slight different linear nature than the triangular nature.[34] The retained stability is a curial factor in supercapacitor applications. The suitable incorporation of the carbon-based rGO materials solve this problem effectively along with PVP, forming the well-shaped structure as clearly evidenced in the selected area of EDAX and TEM images. Figure 5i indicates the cyclic stability graph of the best performed Cu_2FeSnS_4/

https://doi.org/10.1021/acsomega.0c06167
ACS Omega 2021, 6, 9471–9481

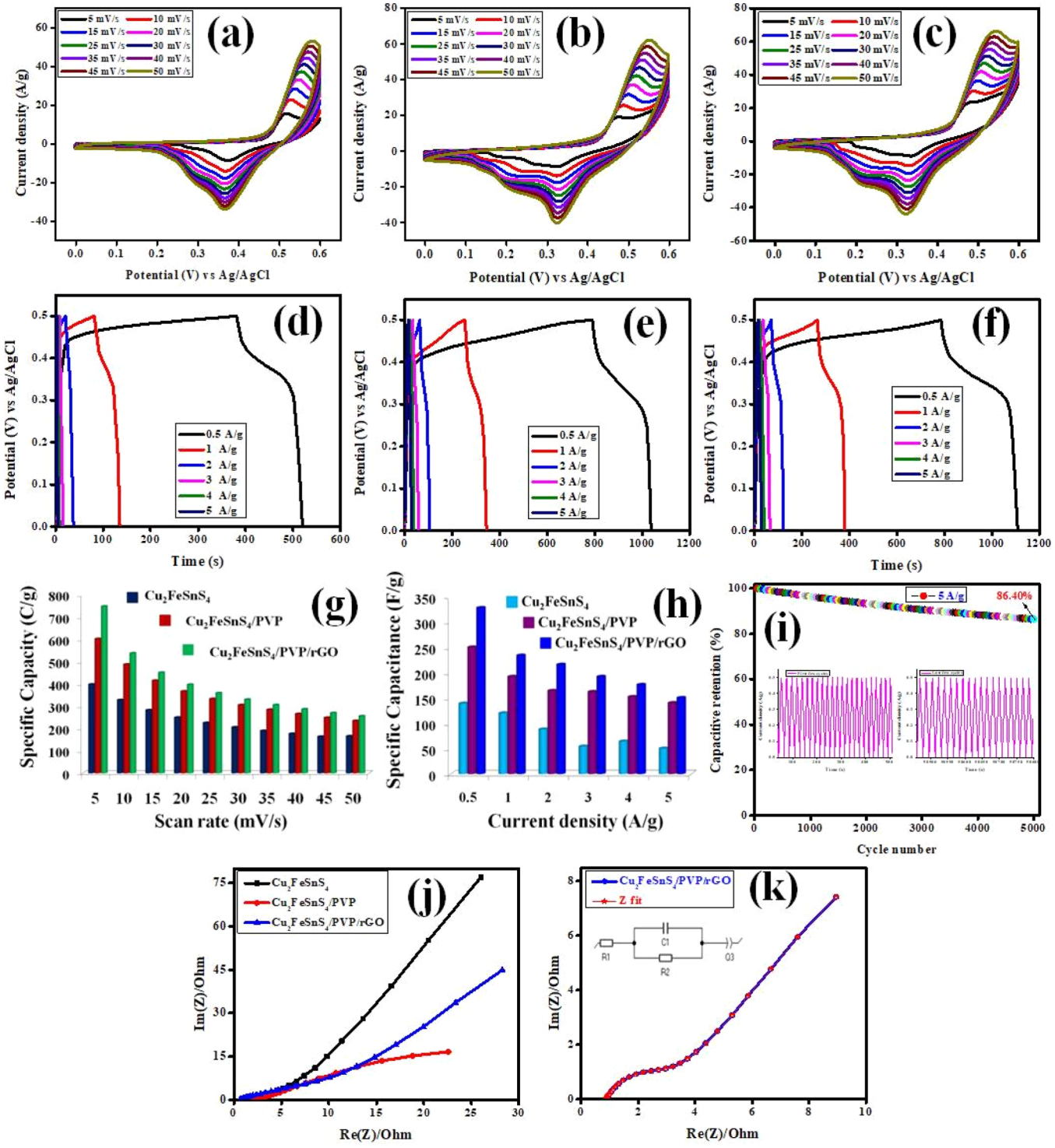

Figure 5. (a–c) CV, (d–f) GCD curves, (g) cone diagram of specific capacity, (h) cone diagram of specific capacitance, (i) capacitive retention of Cu_2FeSnS_4/PVP/rGO, (j) Nyquist plot, and (k) Z-fit graph with the equivalent circuit.

PVP/rGO electrode. The 86.40% of capacity was retained over the 5000 charge–discharge cycles.

EIS analysis was used to evaluate the charge-transfer characteristic of three electrodes (Figure 5j). Furthermore, the addition of rGO in the Cu_2FeSnS_4/PVP/rGO electrode enhances the low charge-transfer resistance which improved electronic conductivity of the prepared electrodes. Equivalent series resistance (ESR) consisting of electrolyte resistance, substrate/active material contact resistance, and internal resistance has been located at the joint in the real part at high frequency expanse in the Nyquist plot. Equivalent charge-transfer resistance (R_{ct}) and solution resistance (R_s) and other phase elements (Q_3) values are summarized in Table 1. The incorporation of rGO increased the adhesion and facilitates charge transport between rGO and Ni foam current collector.[35] It has been fitted using Z fit analysis in biologic SP-150 instrument according to the equivalent circuit, as shown in Figure 5k. The lowest solution resistance shows that

https://doi.org/10.1021/acsomega.0c06167
ACS Omega 2021, 6, 9471–9481

Table 1. Z Fit Analysis of the Nyquist Plot

	equivalent circuit: $R_1 + C_1/R_2 + Q_3$			
parameter	Cu_2FeSnS_4	Cu_2FeSnS_4/PVP	Cu_2FeSnS_4/PVP/rGO	unit
$R_1 = R_s$	0.9016	0.8728	0.6237	Ohm
C_1	0.0294	0.4135×10^{-3}	2.021×10^{-3}	F
$R_2 = R_{ct}$	2.16	2.73	3.77	Ohm
Q_3	0.0408	0.047	0.02633	$F{\cdot}s^{(a-1)}$
a_3	0.4447	0.486	0.5313	

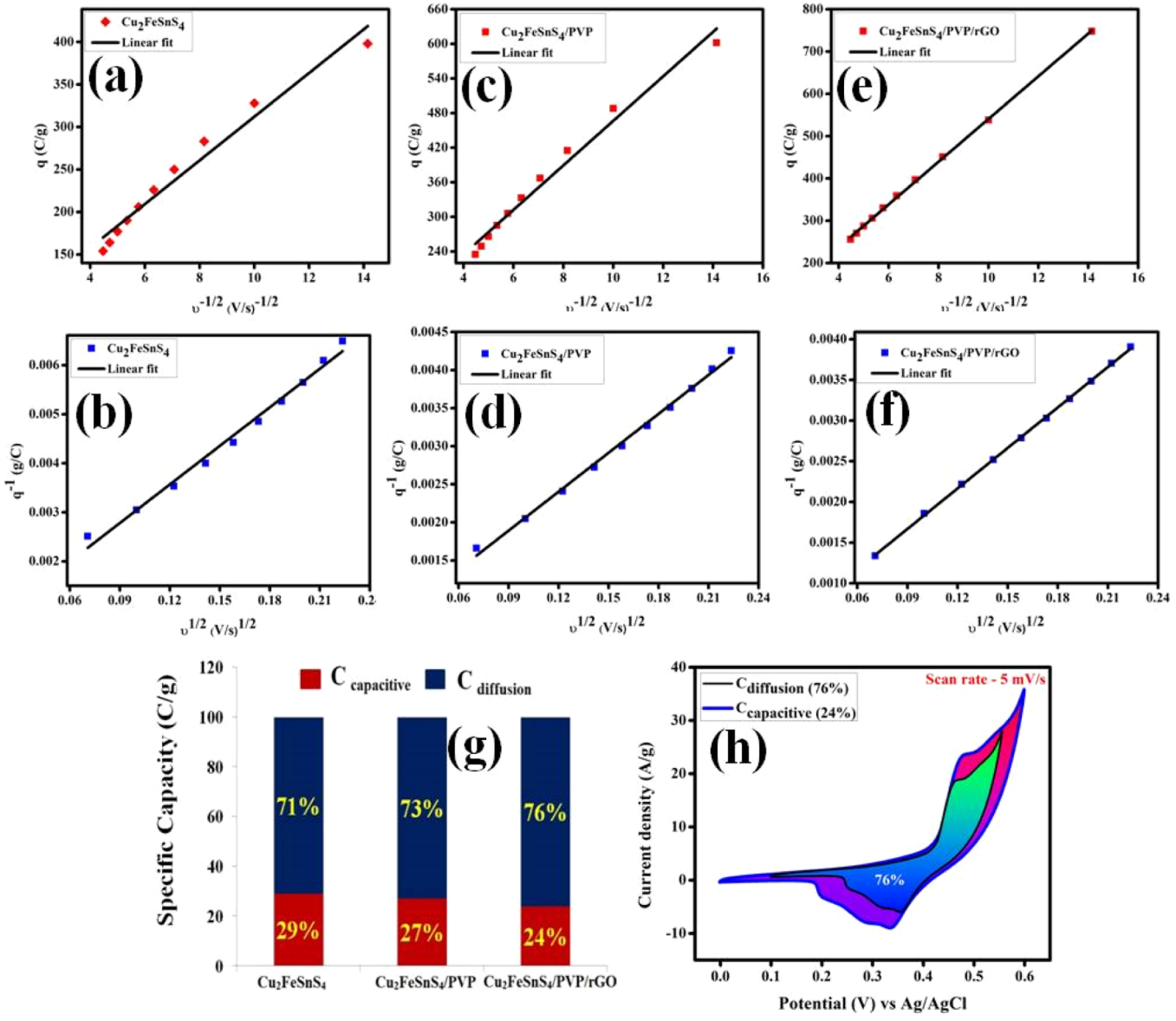

Figure 6. (a,c,e) Specific capacity (C_q); (b,d,f) reciprocal specific capacity ($C_q - 1$); (g) bar diagram of Cu_2FeSnS_4, Cu_2FeSnS_4/PVP, and Cu_2FeSnS_4/PVP/rGO; and (h) $C_{diffusion}$@5 mV/s.

the synthesized Cu_2FeSnS_4/PVP/rGO electrode provides the superior conductivity.

3.1. Trasatti Method. The Trasatti method is used to evaluate capacitive contribution from electrical double-layer and pseudocapacitive reactions. The detailed procedure and the method of calculations are clearly mentioned in our previous work.[36] The capacitive and diffusive contributions in terms of the specific capacity in percentages of all the electrodes are shown in Figure 5g. Figure 5h displays the capacitive- and diffusion-controlled contributions calculated from CV scans at 5 mV/s for the best-performing Cu_2FeSnS_4/PVP/rGO electrode.[37]

3.2. Two-Electrode Device Performances. The two-electrode hybrid device has been fabricated, and the ASC device was assembled with Cu_2FeSnS_4/PVP/rGO as the cathode and AC as the anode, with positive and negative electrodes marked as Cu_2FeSnS_4/PVP/rGO//AC ASC.[38] In fact, the asymmetric and hybrid supercapacitors are the same;

https://doi.org/10.1021/acsomega.0c06167
ACS Omega 2021, 6, 9471−9481

Table 2. Electrochemical Parameters

potential window (V)	current (A)	specific capacitance (F g^{-1})	discharge time (s)	energy density (W h kg^{-1})	power density (W kg^{-1})
1.5	1	234	351	73	749
	2	195	146	61	1504
	3	136	68	43	2276
	5	113	34	35	3705
	10	106	16	33	7425
	15	90	9	28	11,200
	20	66	5	21	15,120

nevertheless, they differ in the appropriate electrode configuration based on their mechanisms. In both cases, EDLC and pseudocapacitive or battery-type properties are explored. The role of the prepared electrode is to increase the energy density by increasing the working voltage without significantly reducing the power density. In our case, the CV curves exhibit the pair of oxidation and reduction which shows the battery-type behavior. The battery-type electrode material combined with the EDLC-based activated carbon material will be termed as the hybrid device, whereas in the case of asymmetric, two different capacitive mechanisms such as EDLC and pseudocapacitance are combined. The electrolyte is the crucial factor to determine the potential window. In general, the aqueous electrolytes have a maximum potential window up to 1 V. The polymer electrolyte may have the potential up to 4 V. In addition to that, the three-electrode and two-electrode system measurement varies in different ways such as $E_{(work)} - E_{(ref)}$ for the three-electrode system and $E_{(work)} - E_{(aux)}$ for the two-electrode system. Hence, for both two-electrode and three-electrode system, working voltage was dependent on the electrode configuration. In our case, we have fixed the potential 1.5 V to evaluate the device performances by varying the scan rate and current density in CV and GCD, respectively. To make an asymmetric device, we used Cu_2FeSnS_4 material as the active cathode and activated carbon as an anode. In between, filter paper was used as a separator. When we optimize device working voltage, we need to take the sum of the voltage differences. The difference of the negative electrode is 1 V and the positive electrode is 0.5 V in GCD. Hence, the sum of the 1.5 V is estimated to evaluate the device performances. We also tested with higher potentials. Nevertheless, the CV graph revealed the oxidation hump in the higher voltages greater than 1.5 V. Hence, we optimize the 1.5 V to evaluate the device performances. Figure 6a explores CV of the positive electrode (0−0.6 V) and negative electrode (−1.0−0 V) at 10 mV/s. Figure 6b displays CV of the ASC hybrid device with different scan rates over a wide potential window up to 1.5 V. Figure 6c shows the GCD profile of the ASC hybrid device with various current densities between 1 and 20 A/g. The fabricated ASC hybrid device revealed the 73 W h/kg and 749 W/kg energy and power density, respectively. Table 2 explores electrochemical device performances of the

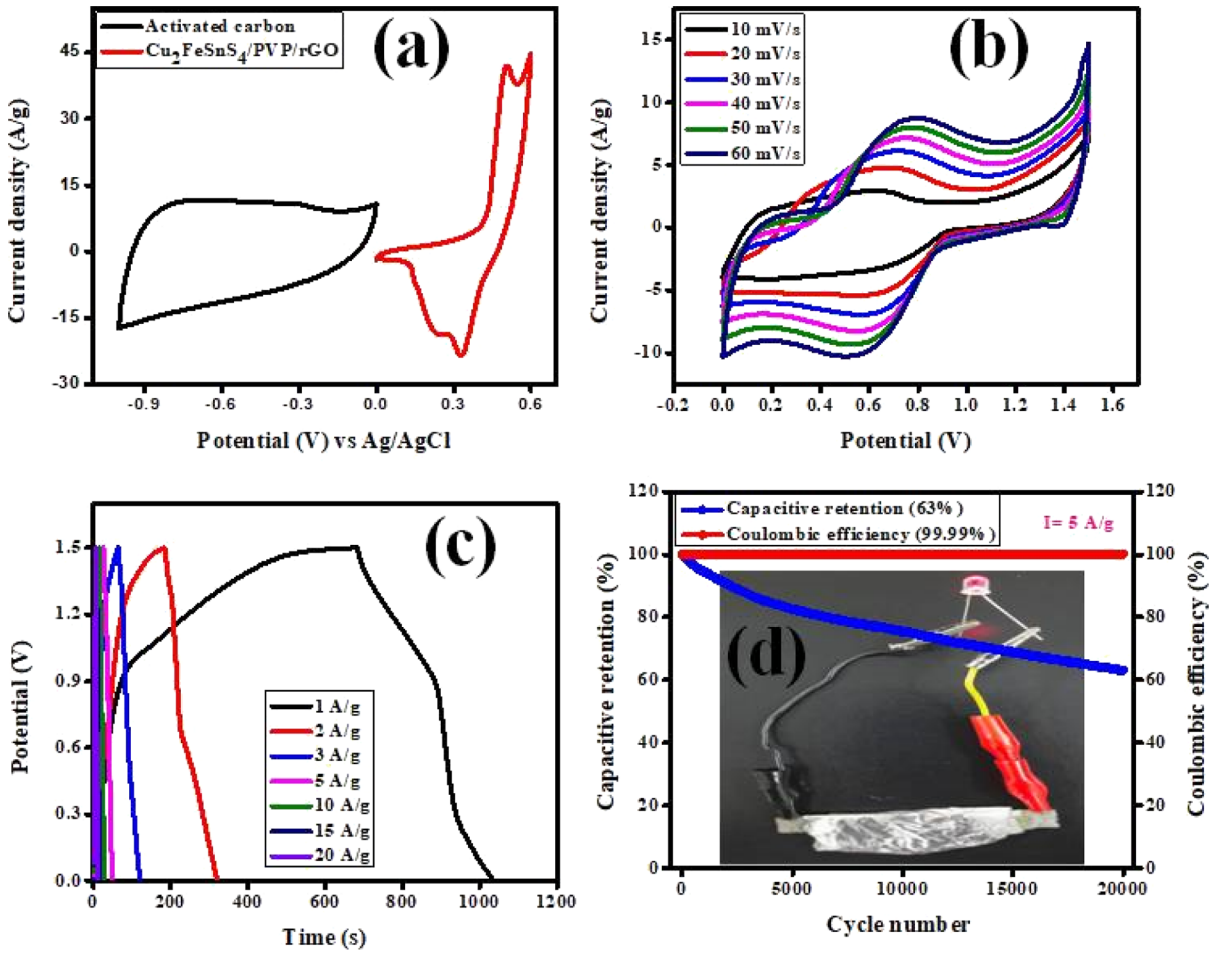

Figure 7. (a) Comparative graph, (b) CV, (c) GCD, and (d) stability graph of the hybrid device.

https://doi.org/10.1021/acsomega.0c06167
ACS Omega 2021, 6, 9471−9481

Table 3. Comparison Table for Cu_2FeSnS_4

positive material//negative material	cell configuration	capacitive retention@ CDcycles	electrolyte	specific capacitance@GCD	energy density (W h kg^{-1})	power density (W kg^{-1})	ref.
$CuFeS_2$//$CuFeS_2$	symmetric device	92.03%@3000	1 M LiOH	34.18 F g^{-1}@1 A g^{-1}	4.74	166	39
$CuCo_2S_4$/CC//AC	asymmetric solid-state device	78.4@3000	PVA/KOH	166.67 mA h g^{-1}@1 A g^{-1}	17.12	194.4	40
CuS-AC//AC	asymmetric device	92%@5000	6 M KOH	247 F g^{-1}@0.5 A g^{-1}	24.88	800	41
Cu_7Se_4−$CuxCo_{1-x}Se_2$	asymmetric device	94.1%@5000	3 M KOH	98.6 F g^{-1}@1 A g^{-1}	26.84	700	42
CuS@CD-GOH//GO	asymmetric device	90%@5000	6 M KOH	920 F g^{-1}@1 A g^{-1}	28	700	43
SnS_2/rGO//AC	asymmetric device	95.1%@5000	3 M KOH	94.5 C g^{-1}@1 A g^{-1}	29.06	747.32	44
$CuCo_2S_4$/$CuCo_2O_4$//graphene	asymmetric device	73%@10,000	2 M KOH	90.4 F g^{-1}@1 A g^{-1}	33.2	800	45
Cu_2S@CoS_2//rGO	asymmetric device	104.7%@8000	2 M KOH	1007 F g^{-1}@2 A g^{-1}	35.4	825	46
CuS/7% rGO/AC	hybrid device	94%@2000	6 M KOH	235 C/g@1 A g^{-1}	43	1426	47
Cu_2FeSnS_4/rGO//AC	hybrid device	63%@20,000	2 M KOH	234 F g^{-1}@1 A g^{-1}	73	749	our work

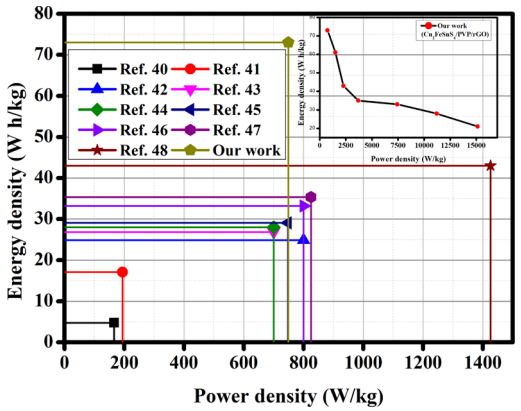

Figure 8. Ragone plot.

ASC hybrid device. The capacitive retention and Columbic efficiency of the fabricated hybrid device are shown in Figure 6d. The small red LED was illuminated with the help of the hybrid device which is inserted in Figure 7d. For the comparison of the energy and power density with our fabricated ASC hybrid device, various reported literature studies are compared, as shown in Table 3. Figure 8 shows the Ragone plot of energy versus power density in comparison with other reported results. In addition, cyclic stability was explored for the Cu_2FeSnS_4/PVP/rGO//AC ASC hybrid device over 2000 charge−discharge cycles at 5 A/g current density in GCD curves. The 63% of capacitive retention and the 99.99% of Coulombic efficiency were retained over 20,000 cycles. The fabricated hybrid device exhibited excellent performance and the cyclic stability which proves the importance of the Cu_2FeSnS_4/PVP/rGO//AC electrode with the energy-storage applications.

4. CONCLUSIONS

In summary, the quaternary Cu_2FeSnS_4/PVP/rGO electrode has been fabricated and used as a potential candidate in supercapacitor application. The remarkable electrochemical performances have been exhibited. The designed Cu_2FeSnS_4/PVP/rGO electrode offers the enhanced conductivity. The active materials of Cu_2FeSnS_4/PVP/rGO revealed an excellent specific capacity of 748 C/g at 5 mV/s in CV and retained 86.40% capacity after 5000 cycles. It exhibits 73W h/kg energy and 749 W/kg power densities. It has a 63% capacity retention and the Coulombic efficiency of 99.99% over 20,000 cycles and explored excellent cyclic stability of the ASC hybrid device. Therefore, this work will serve as a good research electrode material among researchers in the practical need for greater energy use.

AUTHOR INFORMATION

Corresponding Authors

Rathinam Yuvakkumar − *Department of Physics, Alagappa University, Karaikudi 630 003, Tamil Nadu, India*; orcid.org/0000-0001-6779-3453; Email: yuvakkumarr@alagappauniversity.ac.in

Ganesan Ravi − *Department of Physics, Alagappa University, Karaikudi 630 003, Tamil Nadu, India*; Email: raviganesa@rediffmail.com

Dhayalan Velauthapillai − *Faculty of Engineering and Science, Western Norway University of Applied Sciences, Bergen 5063, Norway*; Email: dhayalan.Velauthapillai@hvl.no

Authors

Melkiyur Isacfranklin − *Department of Physics, Alagappa University, Karaikudi 630 003, Tamil Nadu, India*

Balasubramaniam Saravanakumar − *SARP, LARPM, Central Institute of Plastic Engineering and Technology (CIPET), Bhubaneswar 751024, India*

Mehboobali Pannipara − *Department of Chemistry, King Khalid University, Abha 61413, Saudi Arabia*

Abdullah G. Al-Sehemi − *Department of Chemistry, King Khalid University, Abha 61413, Saudi Arabia*

Complete contact information is available at: https://pubs.acs.org/10.1021/acsomega.0c06167

Notes

The authors declare no competing financial interest.

https://doi.org/10.1021/acsomega.0c06167
ACS Omega 2021, 6, 9471−9481

■ ACKNOWLEDGMENTS

This work was supported by UGC-SAP, DST-FIST, DST-PURSE, and MHRD-RUSA grants. The authors are thankful to the Deanship of Scientific Research at King Khalid University for funding this work through Research Group Project under grant number R.G.P.1/35/42. Thanks to Open Access Funding (OA-fond) (oa-fond@hvl.no) at Western Norway University of Applied Sciences, Norway.

■ REFERENCES

(1) Guo, S.; Guo, B.; Ma, R.; Zhu, Y.; Wang, J. KOH activation of coal-derived microporous carbons for oxygen reduction and supercapacitors. *RSC Adv.* **2020**, *10*, 15707−15714.
(2) González, L. G.; Chacon, R.; Delgado, B.; Benavides, D.; Espinoza, J. Study of Energy Compensation Techniques in Photovoltaic Solar Systems with the Use of Supercapacitors in Low-Voltage Networks. *Energies* **2020**, *13*, 3755.
(3) Zheng, Y.; Wang, H.; Sun, S.; Lu, G.; Liu, H.; Huang, M.; Shi, J.; Liu, W.; Li, H. Sustainable nitrogen-doped carbon electrodes for use in high-performance supercapacitors and Li-ion capacitors. *Sustainable Energy Fuels* **2020**, *4*, 1789−1800.
(4) El Sharkawy, H. M.; Sayed, D. M.; Dhmees, A. S.; Aboushahba, R. M.; Allam, N. K. Facile Synthesis of Nanostructured Binary Ni-Cu Phosphides as Advanced Battery Materials for Asymmetric Electrochemical Supercapacitors. *ACS Appl. Energy Mater.* **2020**, *3*, 9305−9314.
(5) Isacfranklin, M.; Rani, B. J.; Ravi, G.; Yuvakkumar, R.; Hong, S. I.; Velauthapillai, D.; Saravanakumar, B. Hydrothermal Method-Derived MnMoO 4 Crystals: Effect of Cationic Surfactant on Microstructures and Electrochemical Properties. *ChemistrySelect* **2020**, *5*, 7728−7733.
(6) Kumar, S.; Saeed, G.; Zhu, L.; Hui, K. N.; Kim, N. H.; Lee, J. H. 0D to 3D carbon-based networks combined with pseudocapacitive electrode material for high energy density supercapacitor: A Review. *Chem. Eng. J.* **2020**, *403*, 126352.
(7) Chodankar, N. R.; Patil, S. J.; Rama Raju, G. S.; Lee, D. W.; Dubal, D. P.; Huh, Y. S.; Han, Y. K. Two-Dimensional Materials for High-Energy Solid-State Asymmetric Pseudocapacitors with High Mass Loadings. *ChemSusChem* **2020**, *13*, 1582.
(8) Xia, L.; Li, X.; Wu, Y.; Hu, S.; Liao, Y.; Huang, L.; Qing, Y.; Lu, X. Electrodes derived from carbon fiber-reinforced cellulose nanofiber/multiwalled carbon nanotube hybrid aerogels for high-energy flexible asymmetric supercapacitors. *Chem. Eng. J.* **2020**, *379*, 122325.
(9) Gopalakrishnan, A.; Raju, T. D.; Badhulika, S. Green synthesis of nitrogen, sulfur-co-doped worm-like hierarchical porous carbon derived from ginger for outstanding supercapacitor performance. *Carbon* **2020**, *168*, 209−219.
(10) Li, Z.; Guo, D.; Liu, Y.; Wang, H.; Wang, L. Recent advances and challenges in biomass-derived porous carbon nanomaterials for supercapacitors. *Chem. Eng. J.* **2020**, *397*, 125418.
(11) Xiong, S.; Jiang, S.; Wang, J.; Lin, H.; Lin, M.; Weng, S.; Liu, S.; Jiao, Y.; Xu, Y.; Chen, J. A high-performance hybrid supercapacitor with NiO derived NiO@Ni-MOF composite electrodes. *Electrochim. Acta* **2020**, *340*, 135956.
(12) Asaithambi, S.; Sakthivel, P.; Karuppaiah, M.; Balamurugan, K.; Yuvakkumar, R.; Thambidurai, M.; Ravi, G. Synthesis and characterization of various transition metals doped SnO2@MoS2 composites for supercapacitor and photocatalytic applications. *J. Alloys Compd.* **2021**, *853*, 157060.
(13) Yilmaz, E. U.; Torbali, M. E. Synergistic effect of biomass-derived carbon and conducting polymer coatings on the supercapacitive energy storage performance of TiO_2. *Mater. Test.* **2020**, *62*, 814−819.
(14) Maity, C. K.; Goswami, N.; Verma, K.; Sahoo, S.; Nayak, G. C. A facile synthesis of boron nitride supported zinc cobalt sulfide nano hybrid as high-performance pseudocapacitive electrode material for asymmetric supercapacitors. *J. Energy Storage* **2020**, *32*, 101993.
(15) Isacfranklin, M.; Yuvakkumar, R.; Ravi, G.; Hong, S. I.; Shini, F.; Thambidurai, M.; Dang, C.; Velauthapillai, D. Marigold flower like structured Cu_2NiSnS_4 electrode for high energy asymmetric solid state supercapacitors. *Sci. Rep.* **2020**, *10*, 19198.
(16) Nefzi, C.; Souli, M.; Cuminal, Y.; Kamoun-Turki, N. Effect of substrate temperature on physical properties of Cu2FeSnS4 thin films for photocatalysis applications. *Mater. Sci. Eng. B* **2020**, *254*, 114509.
(17) El Radaf, I. M.; Al-Zahrani, H. Y. S.; Fouad, S. S.; El-Bana, M. S. Profound optical analysis for novel amorphous Cu_2FeSnS_4 thin films as an absorber layer for thin film solar cells. *Ceram. Int.* **2020**, *46*, 18778.
(18) Giaccherini, A.; Griesi, A.; Montegrossi, G.; Romanelli, M.; Lepore, G. O.; Lavacchi, A.; Amthauer, G.; Redhammer, G.; Tippelt, G.; Martinuzzi, S.; Cucinotta, G.; Mannini, M.; Caneschi, A.; Di Benedetto, F. A new solvothermal approach to obtain nanoparticles in the Cu3SnS4-Cu2FeSnS4 join. *J. Geosci.* **2020**, *65*, 3−14.
(19) Jaiswal, R.; Agarwal, K.; Pratap, V.; Soni, A.; Kumar, S.; Mukhopadhyay, K.; Eswara Prasad, N. Microwave-assisted preparation of magnetic ternary core-shell nanofiller (CoFe2O4/rGO/SiO2) and their epoxy nanocomposite for microwave absorption properties. *Mater. Sci. Eng. B* **2020**, *262*, 114711.
(20) Rani, B. J.; Ravi, G.; Yuvakkumar, R.; Ravichandran, S.; Ameen, F.; AlNadhary, S. Sn doped α-Fe_2O_3 (Sn= 0, 10, 20, 30 wt%) photoanodes for photoelectrochemical water splitting applications. *Renewable Energy* **2019**, *133*, 566−574.
(21) Karuppaiah, M.; Akilan, R.; Sakthivel, P.; Asaithambi, S.; Shankar, R.; Yuvakkumar, R.; Hayakawa, Y.; Ravi, G. Synthesis of self-assembled micro/nano structured manganese carbonate for high performance, long lifespan asymmetric supercapacitors and investigation of atomic-level intercalation properties of OH− ions via first principle calculation. *J. Energy Storage* **2020**, *27*, 101138.
(22) Isacfranklin, M.; Yuvakkumar, R.; Ravi, G.; Hong, S. I.; Velauthapillai, D.; Thambidurai, M.; Dang, C.; Algarni, T. S.; Al-Mohaimeed, A. M. Heterostructured SmCoO3/rGO composite for high-energy hybrid supercapacitors. *Carbon* **2021**, *172*, 613.
(23) Zhou, J.; Yu, S.; Guo, X.; Wu, L.; Li, H. Preparation and characterization of Cu2FeSnS4 thin films for solar cells via a co-electrodeposition method. *Curr. Appl. Phys.* **2019**, *19*, 67−71.
(24) Ajibade, P. A.; Botha, N. L. Synthesis and structural studies of copper sulfide nanocrystals. *Results Phys.* **2016**, *6*, 581−589.
(25) Kumar, S. S.; Khadar, M. A.; Nair, K. G. M. Analysis of the effect of annealing on the photoluminescence spectra of Cu+ ion implanted ZnS nanoparticles. *J. Lumin.* **2011**, *131*, 786−789.
(26) Waluś, E.; Manecki, M.; Cios, G. Synthesis and Characterization of Cu_2FeSnS_4−Cu_2MnSnS_4 Solid Solution Microspheres. *Materials* **2020**, *13*, 4440.
(27) Miao, X.; Chen, R.; Cheng, W. Synthesis and characterization of Cu 2 FeSnS 4 thin films prepared by electrochemical deposition. *Mater. Lett.* **2017**, *193*, 183−186.
(28) Maheskumar, V.; Vidhya, B. Investigation on the morphology and photocatalytic activity of Cu3SnS4 synthesized by ball milling and solvothermal method. *J. Photochem. Photobiol., A* **2018**, *356*, 521−529.
(29) Mokurala, K.; Bhargava, P.; Mallick, S. Single step synthesis of chalcogenide nanoparticles Cu2ZnSnS4, Cu2FeSnS4 by thermal decomposition of metal precursors. *Mater. Chem. Phys.* **2014**, *147*, 371−374.
(30) Cao, M.; Li, C.; Zhang, B.; Huang, J.; Wang, L.; Shen, Y. PVP assisted solvothermal synthesis of uniform Cu2FeSnS4 nanospheres. *J. Alloys Compd.* **2015**, *622*, 695−702.
(31) Baláž, P.; Baláž, M.; Sayagués, M. J.; Eliyas, A.; Kostova, N. G.; Kaňuchová, M.; Dutková, E.; Zorkovská, A. Chalcogenide quaternary Cu_2FeSnS_4 nanocrystals for solar cells: explosive character of mechanochemical synthesis and environmental challenge. *Crystals* **2017**, *7*, 367.
(32) Sahoo, M. K.; Gusain, M.; Thangriyal, S.; Nagarajan, R.; Rao, G. R. Energy storage study of trimetallic Cu2MSnS4 (M: Fe, Co, Ni) nanomaterials prepared by sequential crystallization method. *J. Solid State Chem.* **2020**, *282*, 121049.

https://doi.org/10.1021/acsomega.0c06167
ACS Omega 2021, 6, 9471−9481

(33) Isacfranklin, M.; Ravi, G.; Yuvakkumar, R.; Kumar, P.; Velauthapillai, D.; Saravanakumar, B.; Thambidurai, M.; Dang, C. Urchin like $NiCo_2O_4$/rGO nanocomposite for high energy asymmetric storage applications. *Ceram. Int.* **2020**, *46*, 16291.
(34) Feng, F.; Zhao, S.; Liu, R.; Yang, Z.; Shen, Q. NiO Flowerlike porous hollow nanostructures with an enhanced interfacial storage capability for battery-to-pseudocapacitor transition. *Electrochim. Acta* **2016**, *222*, 1160−1168.
(35) Kumar, G. M.; Xiao, F.; Ilanchezhiyan, P.; Yuldashev, S.; Kang, T. W. Enhanced photoelectrical performance of chemically processed SnS2 nanoplates. *RSC Adv.* **2016**, *6*, 99631−99637.
(36) Isacfranklin, M.; Yuvakkumar, R.; Ravi, G.; Velauthapillai, D.; Pannippara, M.; Al-Sehemi, A. G. Superior supercapacitive performances of Cu_2MnSnS_4 asymmetric device. *Nanoscale Adv.* **2020**, *3*, 486.
(37) Kaipannan, S.; Govindarajan, K.; Sundaramoorthy, S.; Marappan, S. Waste Toner-Derived Carbon/Fe3O4 Nanocomposite for High-Performance Supercapacitor. *ACS Omega* **2019**, *4*, 15798−15805.
(38) Muzaffar, A.; Ahamed, M. B.; Deshmukh, K.; Thirumalai, J. A review on recent advances in hybrid supercapacitors: Design, fabrication and applications. *Renew. Sustain. Energy Rev.* **2019**, *101*, 123−145.
(39) Wang, G.; Zhang, M.; Lu, L.; Xu, H.; Xiao, Z.; Liu, S.; Gao, S.; Yu, Z. One-Pot Synthesis of CuS Nanoflower-Decorated Active Carbon Layer for High-Performance Asymmetric Supercapacitors. *ChemNanoMat* **2018**, *4*, 964−971.
(40) Shi, Y.; Sun, L.; Zhang, Y.; Si, H.; Sun, C.; Gu, J.; Gong, Y.; Li, X.; Zhang, Y. SnS2 nanodots decorated on RGO sheets with enhanced pseudocapacitive performance for asymmetric supercapacitors. *J. Alloys Compd.* **2021**, *853*, 156903.
(41) Sahoo, S.; Pazhamalai, P.; Mariappan, V. K.; Veerasubramani, G. K.; Kim, N.-J.; Kim, S.-J. Hydrothermally synthesized chalcopyrite platelets as an electrode material for symmetric supercapacitors. *Inorg. Chem. Front.* **2020**, *7*, 1492−1502.
(42) Gao, M.; Le, K.; Wang, G.; Wang, Z.; Wang, F.; Liu, W.; Liu, J. Core-shell Cu2-xS @ CoS2 heterogeneous nanowire array with superior electrochemical performance for supercapacitor application. *Electrochim. Acta* **2019**, *323*, 134839.
(43) Xie, T.; Gai, Y.; Shang, Y.; Ma, C.; Su, L.; Liu, J.; Gong, L. Self-Supporting CuCo2 S4 Microspheres for High-Performance Flexible Asymmetric Solid-State Supercapacitors. *Eur. J. Inorg. Chem.* **2018**, 4711−4719.
(44) Xu, X.; Liu, Y.; Dong, P.; Ajayan, P. M.; Shen, J.; Ye, M. Mesostructured CuCo2S4/CuCo2O4 nanoflowers as advanced electrodes for asymmetric supercapacitors. *J. Power Sources* **2018**, *400*, 96−103.
(45) El-Hout, S. I.; Mohamed, S. G.; Gaber, A.; Attia, S. Y.; Shawky, A.; El-Sheikh, S. M. High electrochemical performance of rGO anchored CuS nanospheres for supercapacitor applications. *J. Energy Storage* **2021**, *34*, 102001.
(46) De, B.; Kuila, T.; Kim, N. H.; Lee, J. H. Carbon dot stabilized copper sulphide nanoparticles decorated graphene oxide hydrogel for high performance asymmetric supercapacitor. *Carbon* **2017**, *122*, 247−257.
(47) Yang, X.; Chen, X.; Cao, H.; Li, C.; Wang, L.; Wu, Y.; Wang, C.; Li, Y. Rational synthesis of Cu7Se4-CuxCo1-xSe2 double-shell hollow nanospheres for high performance supercapacitors. *J. Power Sources* **2020**, *480*, 228741.

https://doi.org/10.1021/acsomega.0c06167
ACS Omega 2021, 6, 9471−9481